Hot Deformation Behavior and Processing Map of GH901 Superalloy

Rui Ma [1], **Lulu Li** [1], **Ruixue Zhai** [1,*] , **Xiangnan Meng** [2] **and Jun Zhao** [1]

1   Key Laboratory of Advanced Forging & Stamping Technology and Science, Yanshan University, Qinhuangdao 066004, China; mar@ysu.edu.cn (R.M.); 157331538222@163.com (L.L.); zhaojun@ysu.edu.cn (J.Z.)

2   Xinxiang Aviation Industry (Group) Co., Ltd., Xinxiang 453002, China; mengxn2019@163.com

*   Correspondence: zhairuixue@ysu.edu.cn; Tel.: +86-159-3003-2166

Abstract: During the forging process GH901 superalloys easily produce cracks and defects, such as coarse crystals in tissues, which affect the performance of the alloy. Using GH901 nickel-based alloy, high-temperature compression tests at deformation temperatures of 990, 1040, 1090 and 1140 °C were carried out in a Thermecmastor-Z thermal simulator, with strain rates 0.001, 0.01, 0.1 and 1 s^{-1}. Next, the isothermal forging process of a GH901 disc was simulated using DEFORM finite element simulation software. The results showed that with the increase in deformation temperatures and the decrease in strain rates, the flow stress clearly decreased. The flow stress constitutive model of GH901 superalloy under $\varepsilon_{0.3}$ and the flow stress constitutive model for strain compensation were obtained. The processing map was built, and a reasonable range of thermal processing was obtained. Meanwhile, the isothermal forging simulation verified the reliability of the thermal processing range of the alloy.

Keywords: GH901 superalloy; hot deformation behavior; processing map; isothermal forging

1. Introduction

Nickel-based superalloy [1,2] is a kind of superalloy with high strength, good oxidation resistance and gas corrosion resistance in the range of 650–1000 °C. The name derives from the fact that its content is generally more than 50% nickel. The use of this superalloy is widespread across numerous fields, including aerospace, automobile parts manufacturing, and gas hydrate formation. The macroscopic hot deformation behavior of superalloy corresponds with the dynamic recovery and dynamic recrystallization mechanism in the alloy. At present, the hot deformation behavior of a superalloy is mainly studied within a hot compression simulator. By formulating different process parameters to capture the experimental data, the true stress–strain curve of the alloy can be obtained. The analysis of the influence of different deformation parameters on the rheological behavior of the alloy can then be conducted. The hot deformation constitutive equation [3–5] and processing map of the alloy are obtained by constructing the relationship among deformation temperatures, strain rates and deformation amount. The microstructure and machinability of the alloy under hot deformation can be accurately predicted by analyzing the processing map [6–8].

In the 1980s, processing maps were created based on the evaluation of the thermal processing properties of the alloys based on different material models. Ashby et al. [9] jointly studied the influence of process parameters (deformation temperatures, strain rates, deformation amount, etc.) on the hot deformation process of the alloy, and created a hot deformation mechanism diagram on this basis. However, their research mainly focused on the creep mechanism of an alloy, and this mechanism is only applicable to the state of low strain rates. In order to solve the limitations of the Ashby deformation mechanism diagram, Raj et al. [10] flexibly applied the process parameters (deformation temperatures, strain rates, etc.) during the hot deformation process of the alloy to the Ashby processing

map, and created a processing map based on the atomic model. The creation of this processing map was based on the precondition that the alloy material did not fracture and cause tissue damage. However, there are some limitations. For example, this is not suitable for an alloy with a more complex composition. Based on the above research conclusions, Prasad et al. [11] created the Dynamic Material Model (DMM). Subsequently, many researchers [12–16] further improved upon the DMM by superimposing the drawn instability map and power dissipation map together. The processing map based on the DMM was obtained, which made up for the deficiency of both the Ashby processing map, and the Raj processing map.

In order to improve the comprehensive performance of GH901 superalloy, many researchers have studied the subject from various angles. B. Pei [17] studied the relationship between the heat treatment system of the GH901 superalloy and the yield strength, grain size and endurance life at room temperature, which improved the comprehensive properties of the alloy GH901 from different perspectives. H Zhang et al. [18] studied the effects of different aging temperatures on the microstructure and hardness of the GH901 superalloy, and found that although the aging temperature had no obvious effect on the alloy grain size, a greater effect on the hardness of the alloy was observed. S L Duan et al. [19] studied the influence of the forging process on the wear performance of GH901 alloy shaft forgings, and achieved better forging process parameters.

At present, research reports on GH901 superalloy are relatively few. Systematic and in-depth research on the hot deformation behavior of the alloy is also lacking in China. Therefore, this paper deals with GH901 superalloy and tests the material rheological characteristics under different deformation temperatures and strain rates. The constitutive equation of the alloy was constructed by using the classic Arrhenius mathematical model. The processing map was established based on the Dynamic Material Model, and the finite element software DEFORM was used for simulation. The reasonable isothermal forging process parameters of the GH901 plate were obtained, which provided the necessary basis for formulating the process parameters necessary for the hot forming process of GH901 superalloy.

2. Materials and Methods

The test material was GH901 superalloy bar. The superalloy was cast before forging. The chemical composition of GH901 superalloy was listed, as summarized in Table 1. GH901 superalloy is an Austenitic age–hardening alloy based on an Fe-43Ni-12Cr matrix. It contained Ti, Al, Mo and other strengthening elements. Meanwhile, there were traces of boron, carbon elements, the metastable intermetallic compound γ'' [Ni_3(Ti, Al)], and phase diffusion, which strengthened the alloy. The elements of Al could have inhibited the transformation of γ'' to η-Ni_3Ti. The melting point of the alloy was 1360 °C. The density was 8.21 g/cm^3. The alloy was non-magnetic, and similar grades were Nimonic901 (UK), Z8NCDT42 (France), etc. Alloy disc forgings were formed by upsetting and then molding.

Table 1. Chemical composition of GH901 superalloy (wt. %).

C	Mn	Si	Cr	Mo	S	P	Al
0.031	0.00063	0.045	12.43	6.00	0.0006	0.015	0.22
Ti	**Cu**	**Co**	**B**	**Pb**	**Bi**	**Ag**	**Ni+Co**
3.06	0.0030	0.015	0.015	0.00017	0.000043	0.000073	42.28

The original metallographic structure of GH901 superalloy before hot deformation is shown in Figure 1. The matrix was a single-phase austenite structure, and some twinning structures existed in the structure. To clarify, two parts of crystal with the same structure were arranged symmetrically according to a particular orientation relationship.
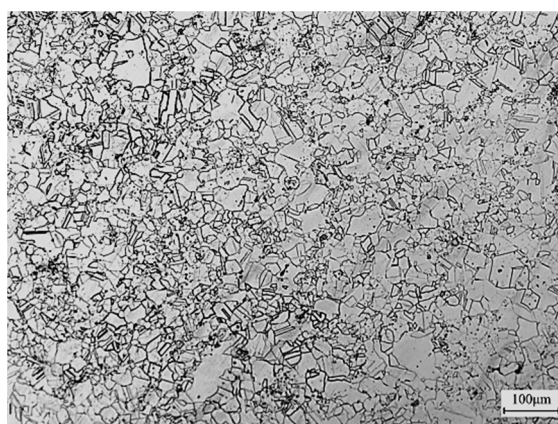
Figure 1. Original metallographic structure of GH901 superalloy.

The high-temperature compression experiment of GH901 superalloy was completed in the Thermecmastor-Z thermal simulator (Aipei Test Equipment, Dongguan, China). First, the cylindrical hot compression sample measuring Ø8 mm × 12 mm was cut out of the Ø250 mm × 172 mm forged GH901 superalloy steel blank using an EDM wire-cutting machine and the lathe, as shown in Figure 2. In order to prevent uneven deformation of the sample during compression, glue was used to attach a mica sheet between the ceramic indenter and the sample, so as to reduce friction. The experimental condition was a vacuum. When the heating temperature of GH901 superalloy was between 1000 °C and 1100 °C, the forging was not easy to crack and had good hot-deformation plasticity [20–22]. Therefore, the deformation temperatures of the compression experiment were set as follows: 990, 1040, 1090, 1140 °C; strain rates, 0.001, 0.01, 0.1, 1 s^{-1}; deformation degree, 50%; heating speed, 10 °C/s; holding time, 60 s; cooling method, the sample after compression deformation is cooled by nitrogen. Figure 3 shows the flow chart of isothermal compression. During this experiment, a Zeiss HAL100 Optical microscope (OM) (Fuji Radio Machinery Co., Ltd., Fuji-shi, Japan) was used to observe the microstructure of the samples.
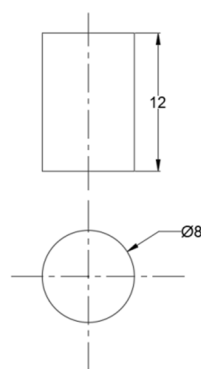

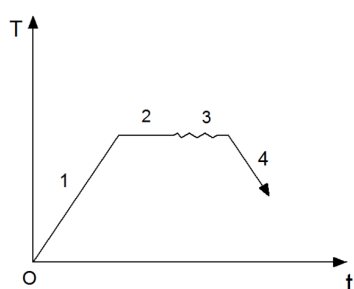**Figure 2.** Original cylindrical specimen.

Figure 3. Flow chart of isothermal compression.

3. Results

3.1. Hot Deformation Behavior

The flow–curves and microstructure of the GH901 superalloy under different deformation temperatures and strain rates are shown in Figures 4–7.
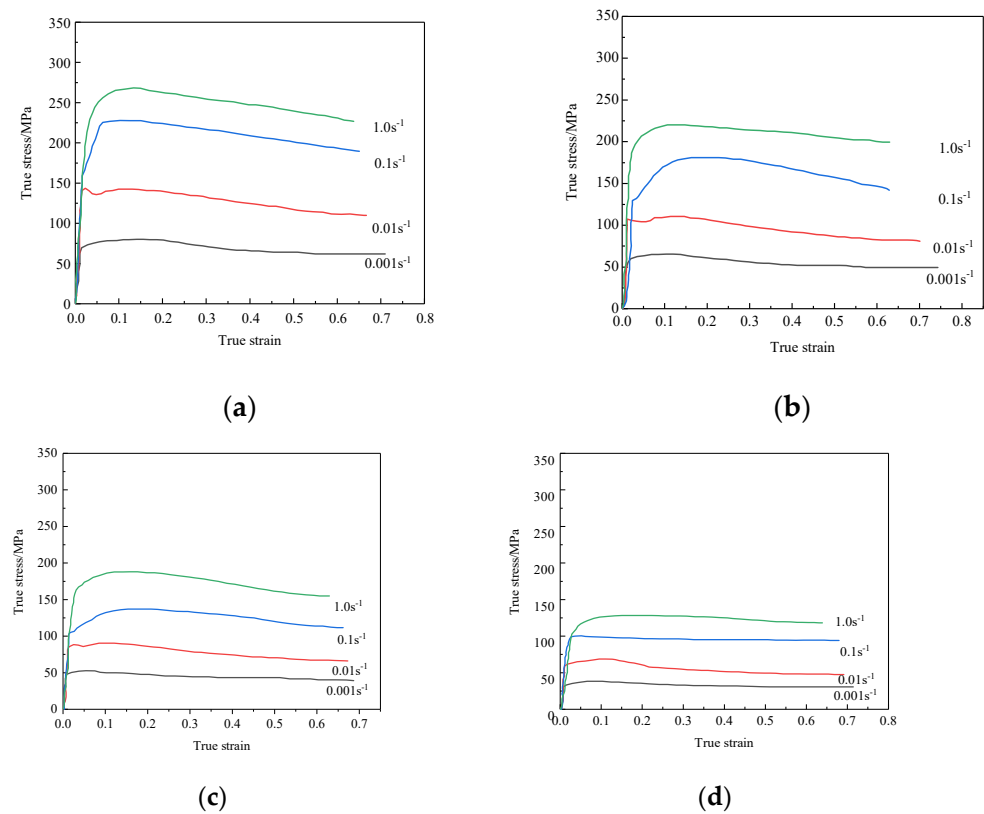

(a)

(b)

(c)

(d)

Figure 4. True stress–strain curves of GH901. (**a**) T = 990 °C, (**b**) T = 1040 °C, (**c**) T = 1090 °C, (**d**) T = 1140 °C.
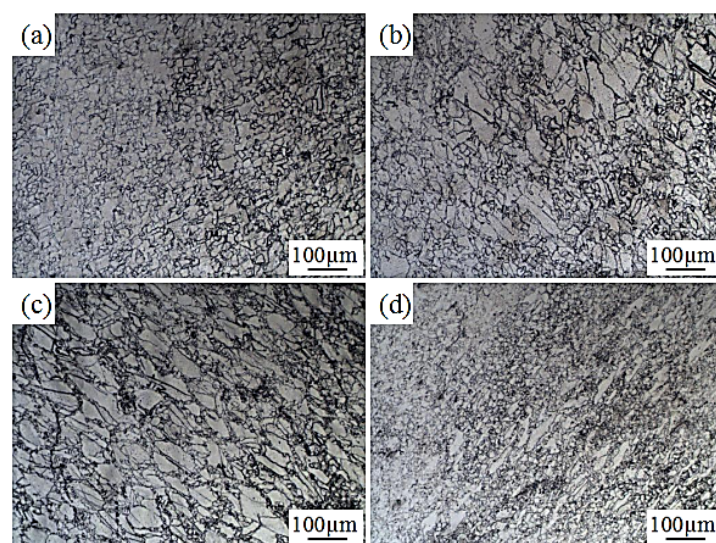
Figure 5. Microstructure of GH901 superalloy deformed at 1090 °C. (**a**) Microstructure at 0.001 s^{-1}, (**b**) Microstructure at 0.01 s^{-1}, (**c**) Microstructure at 0.1 s^{-1}, (**d**) Microstructure at 1 s^{-1}.
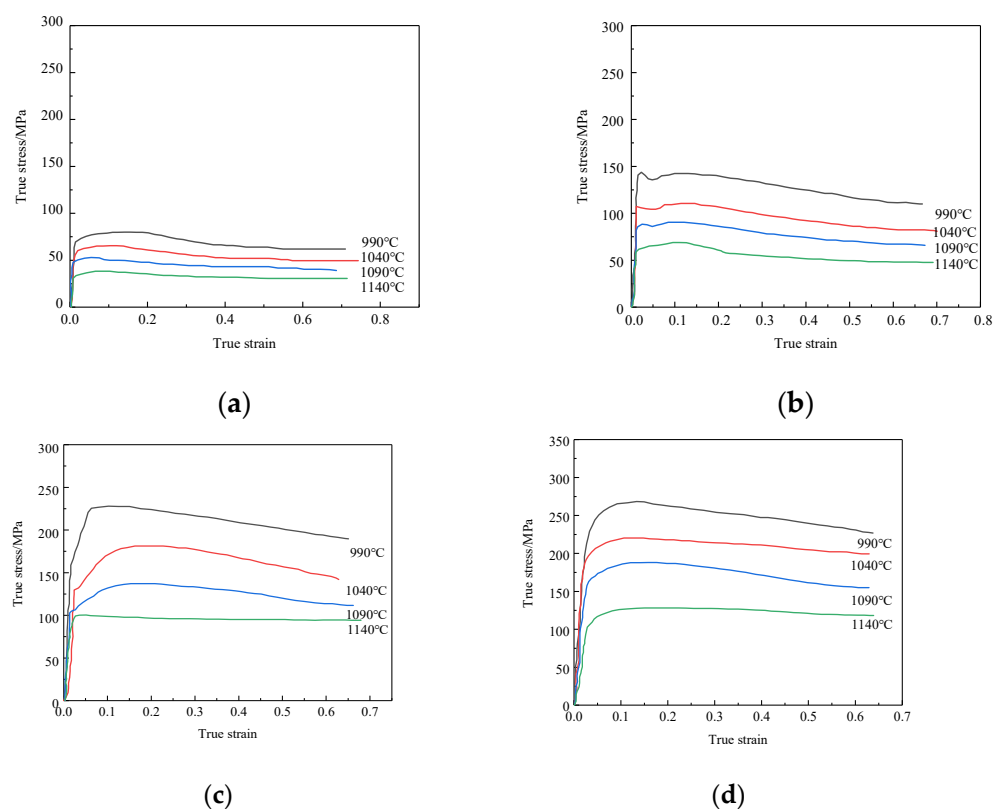
Figure 6. True stress-strain curves of GH901. (**a**) $\dot{\varepsilon} = 0.001\ \mathrm{s}^{-1}$, (**b**) $\dot{\varepsilon} = 0.01\ \mathrm{s}^{-1}$, (**c**) $\dot{\varepsilon} = 0.1\ \mathrm{s}^{-1}$, (**d**) $\dot{\varepsilon} = 1\ \mathrm{s}^{-1}$.

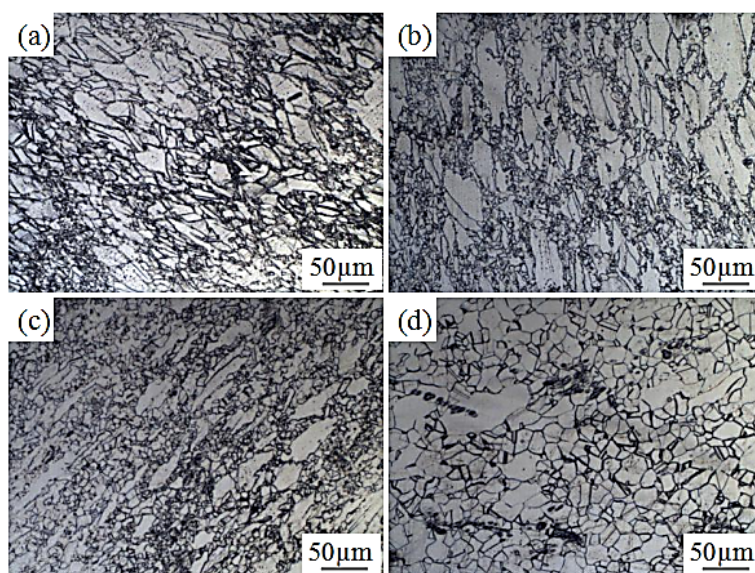**Figure 7.** Microstructure of GH901 superalloy deformed at 1 s^{-1}. (**a**) Microstructure at 990 °C, (**b**) Microstructure at 1040 °C, (**c**) Microstructure at 1090 °C, (**d**) Microstructure at 1140 °C.

Figures 4 and 5 show that, due to the low rate of 0.001 s^{-1}, dynamic recrystallization fully occurred. This formed fine equiaxed structures that absorbed surrounding grains and expanded. At 0.01 s^{-1}, the volume fraction of recrystallized grains significantly decreased, and there were a lot of coarse original grains in the microstructure. At 0.1 s^{-1}, the elongated original deformed grains were retained and a small amount of dynamic recrystallized grains existed around them. At 1 s^{-1}, the volume fraction of recrystallization clearly

increased. Under the same conditions, the same deformation temperature, and using the same time intervals, when the strain rate was higher the degree of plastic deformation of the material was larger. The dislocation density increased, and the work-hardening effect was obvious, which increased the deformation resistance of the material. Under the same strain, due to the high strain rate, fast deformation rate, short dynamic recrystallization and dynamic recovery time, the difference between the softening effect and the hardening effect was large, and the steady state flow stress of the material increased along with the strain rates. At 1 s^{-1}, a large amount of heat was released in a short time during the deformation process, and the thermal effect formed promoted the dynamic recrystallization. The lower strain rate was beneficial to the formation of a substructure, and the dynamic recrystallization nucleation and growth process quickened. Thus, dynamic recrystallization behavior was promoted. Once the softening effect and hardening effect were balanced, the peak stress and corresponding strain value decreased alongside the strain rates.

According to Figures 6 and 7, when the alloy was deformed at 990 °C, part of the microstructure was dynamically recrystallized, and formed fine equiaxed grains. This was surrounded by the original coarse grains, which formed a serrated boundary chain. At 1040 °C, the recrystallized grains further increased and formed a "necklace" shape with an elongated coarse structure. At 1090 °C, the number of recrystallized grains increased and their size grew. At 1140 °C, when compared with the microstructure at 1090 °C, the equiaxed grains formed by recrystallization absorbed the deformed grains and grew upwards. Some irregular coarse grains also existed. With a higher deformation temperature, the softening effect gradually offset the work-hardening effect, the softening effect continued to increase, and the flow stress value of the material decreased. At the same time, the more violent the atomic motion in the alloy and the higher the atomic diffusion rate, the higher the probability of dislocation climb and slip, and dynamic recrystallization. At the same strain rate, the strain value corresponding to the peak stress decreased with the increase in deformation temperature.

3.2. Constitutive Analysis

3.2.1. Establishment of Constitutive Equation

The influence of different deformation conditions on the hot deformation process can be characterized by an exponential equation. The mathematical expressions of the equations are found in Equations (1)–(4). According to the study of Hollomon and Zener [23], the influence of strain rates and deformation temperatures on the hot deformation process can be expressed by a mathematical expression. This contains parameter Z, as Equation (5), and Z is a factor that temperatures compensate the strain rates.

$$\dot{\varepsilon} \;=\; AF(\sigma)\exp[-Q/(RT)], \tag{1}$$

$$F(\sigma) \;=\; \sigma^{n_1} \; (\alpha\sigma < 0.8), \tag{2}$$

$$F(\sigma) \;=\; \exp(\beta\sigma) \; (\alpha\sigma > 1.2), \tag{3}$$

$$F(\sigma) \;=\; [\sinh(\alpha\sigma)]^n, \tag{4}$$

$$Z \;=\; \dot{\varepsilon}\exp(Q/RT). \tag{5}$$

where $F(\sigma)$ is the function of stress,

A, n_1 and β are the material constants, with $\alpha \;=\; \beta/n_1$,
σ is the true stress (MPa),
R is the molar gas constant, and number is 8.314,
T is the temperature (K).

The data with strain value of 0.3 under different deformation conditions were used as the basis for constructing the constitutive model, as shown in Table 2.

Table 2. The corresponding stress when the strain is 0.3 (Mpa).

Deformation Temperature $T/°C$	Strain Rate $\dot{\varepsilon}/s^{-1}$			
	0.001	**0.01**	**0.1**	**1**
990	70.626	132.98	250.98	256.22
1040	55.984	99.08	177.32	212.79
1090	44.17034	78.609	132.82	180.94
1140	33.249	55.046	122.18	125.46

$\ln \sigma_{0.3}$ was as the horizontal axes and $\ln \dot{\varepsilon}$ was as the vertical axes, as shown in Figure 8a,b. Then, linear regression was performed on all curves to obtain the slope of the fitting line at different deformation temperatures, as shown in Table 3.
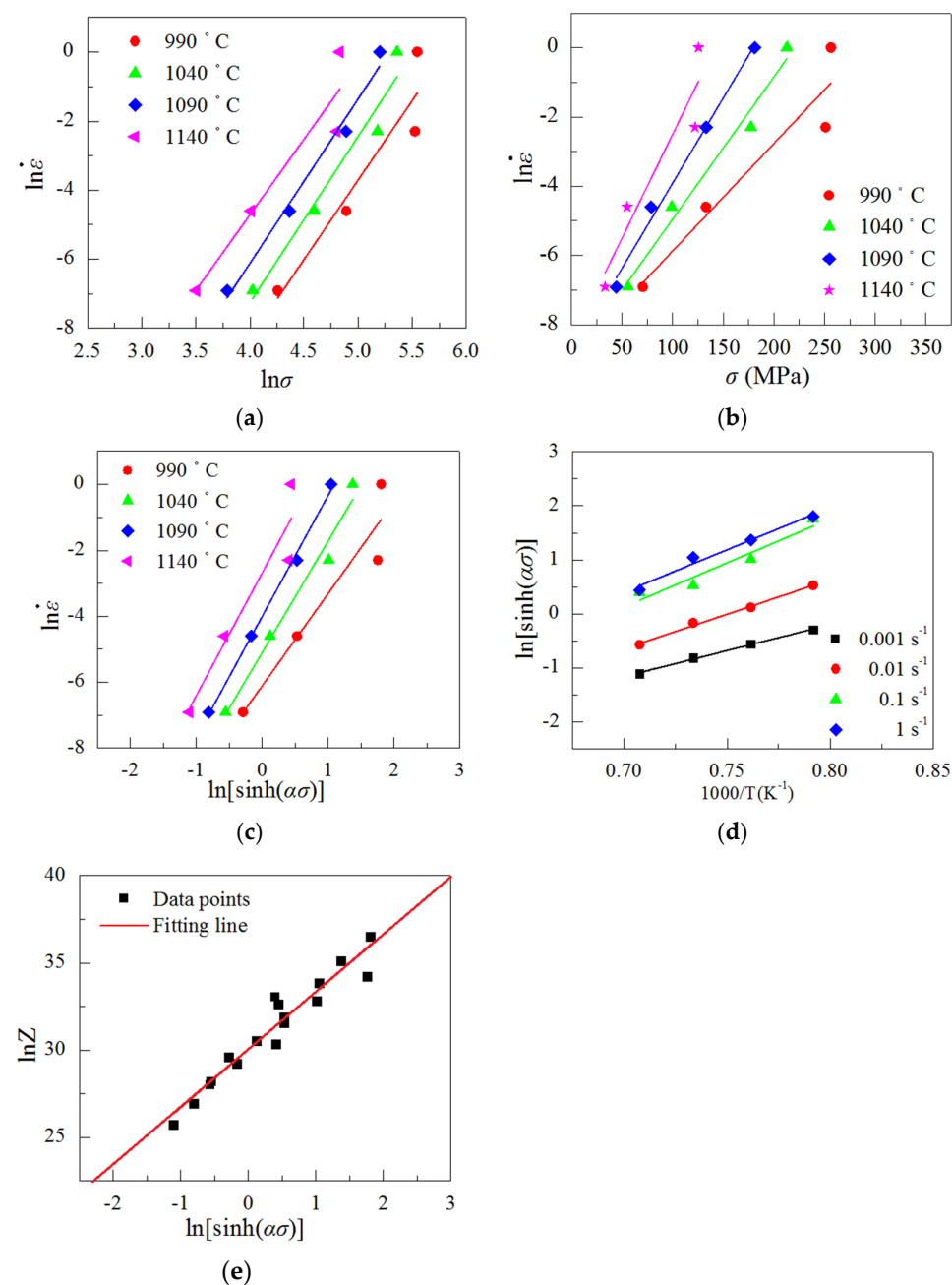

Figure 8. Linear regression curves. (**a**) $\ln \dot{\varepsilon} - \ln \sigma_{0.3}$, (**b**) $\ln \dot{\varepsilon} - \sigma_{0.3}$, (**c**) $\ln \dot{\varepsilon} - \ln[\sinh(\alpha\sigma_{0.3})]$, (**d**) $\ln[\sinh(\alpha\sigma_{0.3})] - \frac{1}{T}$, (**e**) $\ln Z - \ln[\sinh(\alpha\sigma_{0.3})]$.

Table 3. Regression analysis results of $\varepsilon_{0.3}$ and $\dot{\varepsilon}$ under different temperatures.

Material Parameter	Deformation Temperature $T/°C$			
	990	**1040**	**1090**	**1140**
$n_1 : \ln\dot{\varepsilon} - \ln\sigma_{0.3}$	4.60344	4.80803	4.76176	4.38038
$\beta : \ln\dot{\varepsilon} - \sigma_{0.3}$	0.03107	0.0411	0.0492	0.06005

$\ln\dot{\varepsilon} - \ln[\sinh(\alpha\sigma_{0.3})]$ were as the horizontal and vertical axes images rendered, shown as Figure 8c. Linear regression was performed on the curve to obtain the fitting slope of deformation temperature, and the fitting parameters, as summarized in Table 4.

Table 4. The hyperbolic sine function fits the slope of $\dot{\varepsilon}$ and $\varepsilon_{0.3}$ under different deformation conditions.

Material Parameter	Deformation Temperature $T/°C$			
	990	**1040**	**1090**	**1140**
n	2.79443	3.37687	3.66579	3.72341

The average of slope n was 3.390125. By linear regression processing, we could obtain the relation curve of $\ln[\sinh(\alpha\sigma_{0.3})] - \left(\frac{1}{T}\right)$, shown as Figure 8d. The slope of the fitting line at different deformation temperatures is summarized in Table 5. The average thermal activation energy Q of the alloy was $383.5184 \text{ KJ} \cdot \text{mol}^{-1}$. $\ln[\sinh(\alpha\sigma_{0.3})] - \ln Z$ were the horizontal and vertical axes image rendering and could acquire $A = 9.967989 \times 10^{12}$, shown as Figure 8e.

Table 5. The regression analysis results of hyperbolic sine function of temperature and $\varepsilon_{0.3}$.

Material Parameter	Strain Rate $\dot{\varepsilon}/\text{s}^{-1}$			
	0.001	**0.01**	**0.1**	**1**
$\frac{Q}{nR}$	9.61373	12.81344	16.30829	15.68962

By substituting in the calculated material constants Q, A, n, α, we could obtain the kinetic Equation (6) of alloy steel GH901. The flow stress constitutive equation applicable to any stress level state was also obtained, Equation (7).

$$\dot{\varepsilon} = 9.9680 \times 10^{12}[\sinh(0.009779\sigma_{0.3})]^{3.390}\exp[-383518/(RT)], \tag{6}$$

$$\begin{cases} \sigma = (1/0.009779)\ln\left\{(Z/9.9680E^{12})^{(1/3.390)} + \left[(Z/9.9680E^{12})^{(2/3.390)} + 1\right]^{1/2}\right\} \\ Z = \dot{\varepsilon}\exp[383518/(RT)] \end{cases} \tag{7}$$

where E is the Elastic Modulus (GPa).

As shown in Figure 9, the calculated correlation coefficient R between the test value and the predicted value was 0.967, close to the constant 1. The absolute value of the average relative error between the test value and the predicted value, AARE (%) was 9.279%, and therefore within the acceptable margin for error of 10%. Therefore, the flow stress constitutive equation based on strain 0.3 could better predict the flow stress of GH901 alloy material under the conditions of deformation temperatures 990–1140 °C and strain rates 0.001–1 s^{-1}.
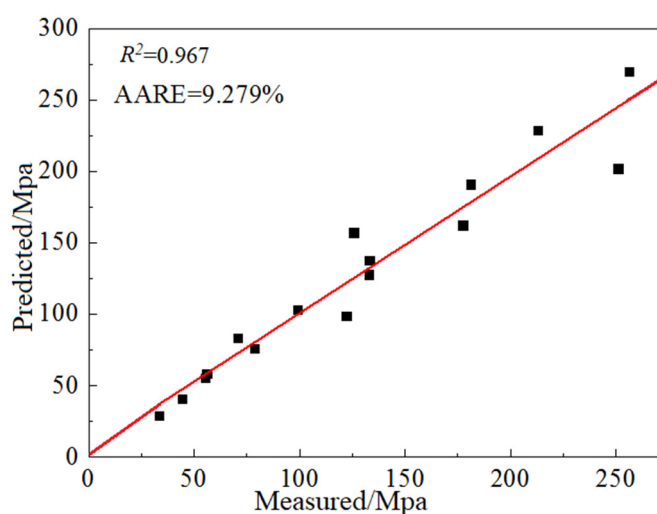
Figure 9. Measured versus the predicted $\varepsilon_{0.3}$.

3.2.2. Construction of Constitutive Model Based on Strain Compensation

The flow stress constitutive equation, which was based on strain 0.3, did not consider the effect of strain on the rheological model. Therefore, in this section, the strain compensation method was used as a comprehensive and accurate flow stress constitutive equation for solving issues with processing maps of GH901 superalloy, such as comprehensive consideration of strain rates, deformation temperatures, deformation of alloy hot forming parameters, and the influence of the flow stress. The corresponding stress value data under different strains (0.05, 0.1, 0.15, 0.2, 0.25, 0.3, 0.35, 0.4, 0.45, 0.5, 0.55, 0.6) were extracted and integrated. The material parameters of the constitutive model corresponding to each strain were solved by linear regression processing, as shown in Table 6.

Table 6. Material parameters Q, n, α and $\ln A$ under different strains.

Strain	α	n	Q/KJ·mol^{-1}	$\ln A$
0.05	0.009956	4.219159	424.2852	33.42577
0.1	0.009368	3.911235	409.8304	32.06992
0.15	0.009136	3.709211	399.5897	31.28004
0.2	0.009176	3.599519	393.6089	30.82849
0.25	0.009526	3.420980	386.5302	30.20629
0.3	0.009779	3.390125	383.5184	29.93040
0.35	0.010049	3.377397	383.7422	29.92981
0.4	0.010337	3.345353	387.0122	30.232746
0.45	0.010514	3.411254	392.0682	30.696745
0.5	0.010743	3.466367	394.5052	30.913938
0.55	0.010999	3.434757	401.3594	31.554777
0.6	0.011112	3.506462	400.0757	31.460104

The data of each group in Table 6 were substituted into Equation (8). Then, the seventh degree polynomial was used in Origin software to fit the relationship between material parameters and strain under various deformation conditions. The fitting image of data for each group is shown in Figure 10.

$$
\begin{cases}
\alpha = \alpha_0 + \alpha_1\varepsilon + \alpha_2\varepsilon^2 + \alpha_3\varepsilon^3 + \alpha_4\varepsilon^4 + \alpha_5\varepsilon^5 + \alpha_6\varepsilon^6 + \alpha_7\varepsilon^7 \\
n = n_0 + n_1\varepsilon + n_2\varepsilon^2 + n_3\varepsilon^3 + n_4\varepsilon^4 + n_5\varepsilon^5 + n_6\varepsilon^6 + n_7\varepsilon^7 \\
Q = Q_0 + Q_1\varepsilon + Q_2\varepsilon^2 + Q_3\varepsilon^3 + Q_4\varepsilon^4 + Q_5\varepsilon^5 + Q_6\varepsilon^6 + Q_7\varepsilon^7 \\
\ln A = a_0 + a_1\varepsilon + a_2\varepsilon^2 + a_3\varepsilon^3 + a_4\varepsilon^4 + a_5\varepsilon^5 + a_6\varepsilon^6 + a_7\varepsilon^7
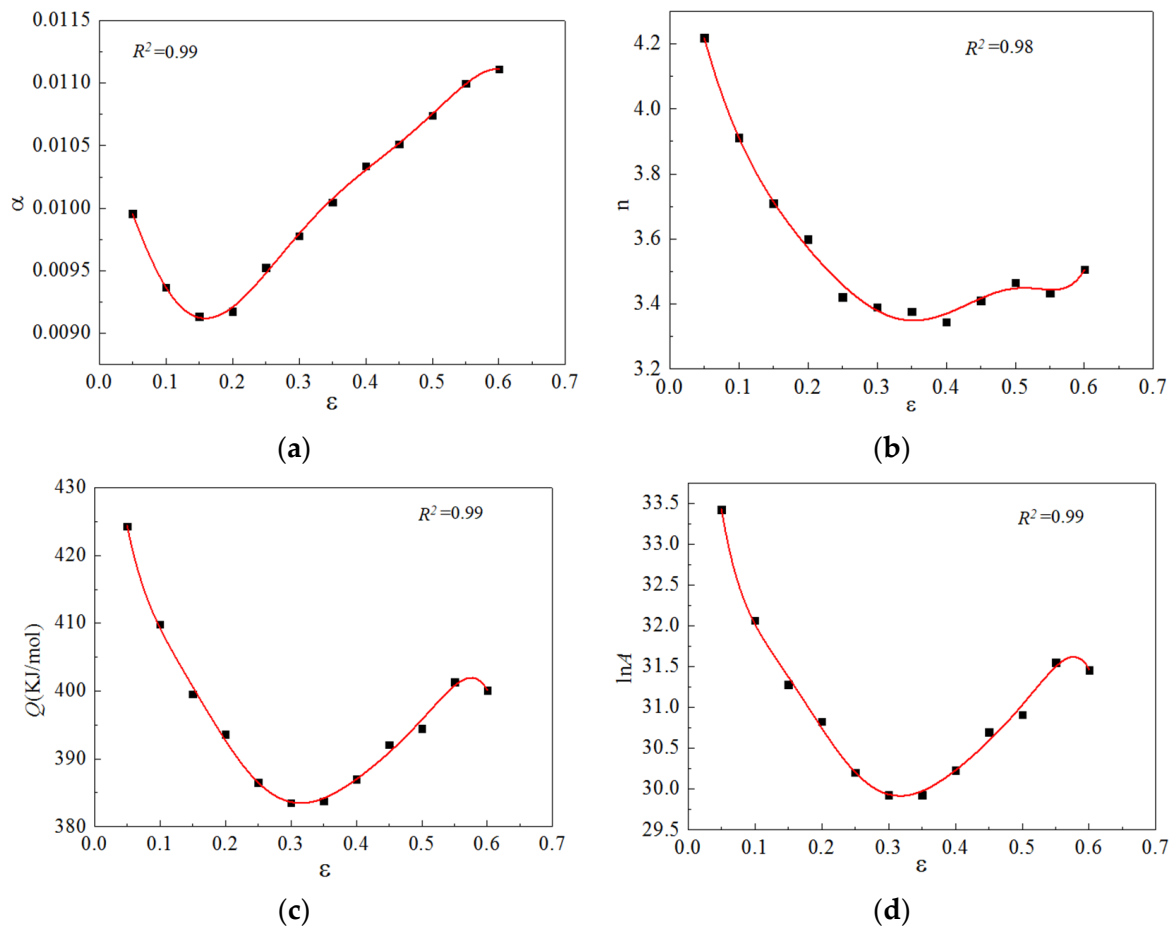\end{cases} \tag{8}
$$

Figure 10. Polynomial relationship between material parameters and strain. (**a**) α, (**b**) n, (**c**) Q, (**d**) $\ln A$.

The flow stress constitutive equation of GH901 superalloy with a comprehensive consideration of deformation temperatures, strain rates and amount of deformation could be obtained from the above calculation, as shown in Equation (9):

$$
\left\{
\begin{aligned}
\alpha &= 0.0106 - 0.0093\varepsilon - 0.1423\varepsilon^2 + 1.6163\varepsilon^3 - 6.0594\varepsilon^4 + 10.815\varepsilon^5 - 9.2018\varepsilon^6 + 2.9228\varepsilon^7 \\
n &= 4.6878 - 11.104\varepsilon + 31.514\varepsilon^2 + 113.54\varepsilon^3 - 1315.0\varepsilon^4 + 4385.0\varepsilon^5 - 6344.8\varepsilon^6 + 3396.4\varepsilon^7 \\
Q &= 469.72 - 1528.6\varepsilon + 17.130\varepsilon^2 - 112.554\varepsilon^3 + 412.151\varepsilon^4 - 833.977\varepsilon^5 + 878.448\varepsilon^6 - 37.7126\varepsilon^7 \\
\ln A &= 38.439 - 172.86\varepsilon + 1991.5\varepsilon^2 - 12.790\varepsilon^3 + 45.592\varepsilon^4 - 90.225\varepsilon^5 + 93.321\varepsilon^6 - 39.450\varepsilon^7 \\
Z &= \dot{\varepsilon}\exp(Q/RT) \\
\sigma &= (1/\alpha)\ln\left\{ (Z/A)^{1/n} + \left[(Z/A)^{2/n} + 1 \right]^{1/2} \right\}
\end{aligned}
\right.
\tag{9}
$$

As can be seen from Figures 11 and 12, under different strains, the absolute value of the average relative error AARE (%) between the tested stress value and the predicted stress value was 8.123%, which was less than the acceptable error range of 10%. Meanwhile, the correlation coefficient R between the tested stress value and the predicted stress value under different strains was 0.992, close to the constant 1. Therefore, the flow stress constitutive equation built under different strain conditions could better realize the prediction of the flow stress of a GH901 nickel-based superalloy under the conditions of deformation temperatures 990–1140 °C and strain rates 0.001–1 s^{-1}.
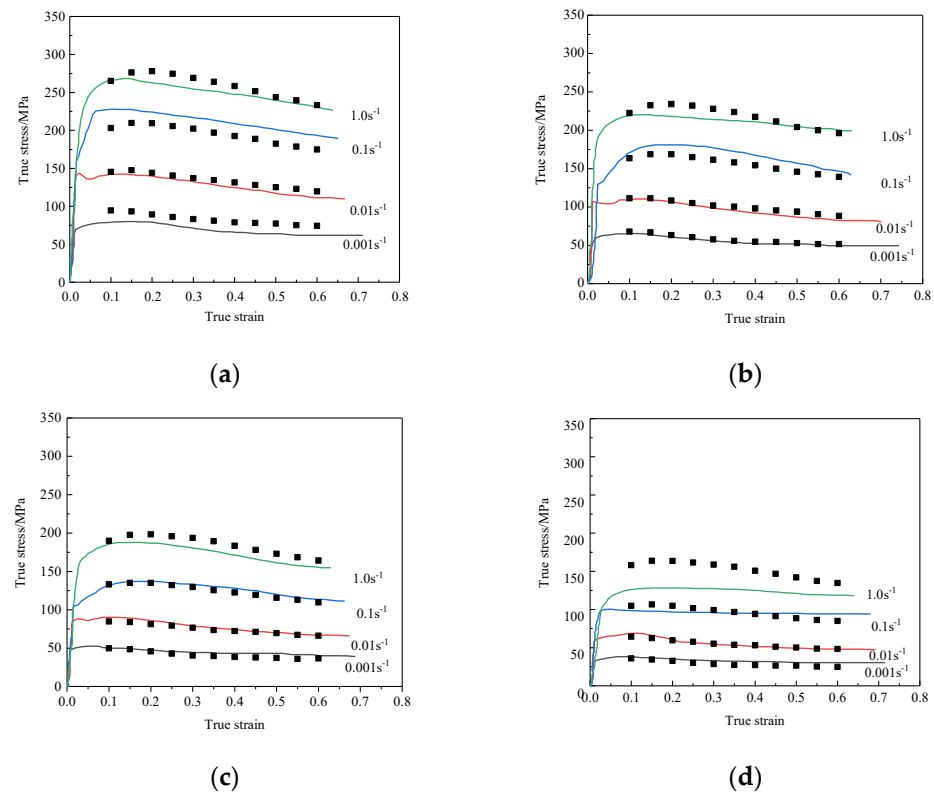
Figure 11. Experimental and calculated data. (**a**) T = 990 °C, (**b**) T = 1040 °C, (**c**) T = 1090 °C, (**d**) T = 1140 °C.
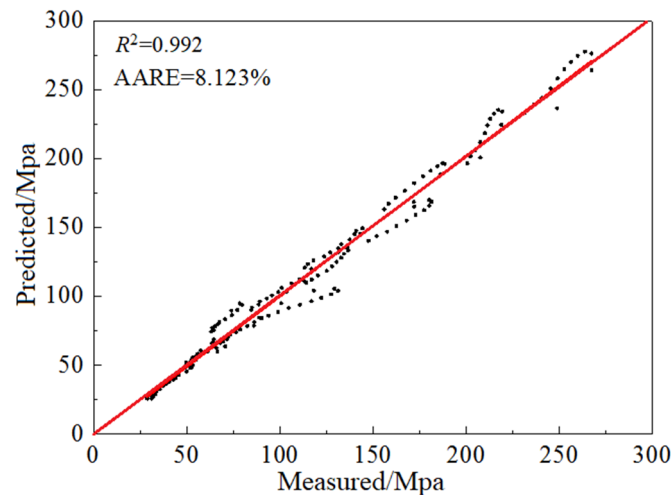

Figure 12. Measured versus the predicted stress.

3.3. Construction of Processing Map

According to the basic principle of the dynamic material model and the established constitutive model, the alloy material can be regarded as a nonlinear energy dissipation system during the hot deformation process. The power dissipation map can be used to reflect the microstructure evolution mechanism of alloy materials during hot deformation, such as dynamic recovery and dynamic recrystallization. The energy dissipation of the tissue after evolution can be expressed by power dissipation efficiency factor η, and can be expressed as follows:

$$\eta = \frac{J}{J_{max}} = \frac{2m}{m+1}, \tag{10}$$

In the equation, η is a dimensionless constant, which changes with the strain rates and deformation temperatures in the hot deformation process. Furthermore, this equation can be used to draw the isolines of alloy materials at different deformation amounts, and then form the power dissipation map.

On the basis of the dynamic material model (DMM), Prasad et al. [11] judged the rheological instability of the material according to the extreme value principle in irreversible thermodynamics, that is, when the power dissipation value J and deformation strain rate $\dot{\varepsilon}$ of the alloy material satisfied the following relation in the hot deformation process:

$$\frac{\partial J}{\partial \dot{\varepsilon}} < \frac{J}{\dot{\varepsilon}}, \tag{11}$$

combined with Equation (11), the decision equation of Prasad's rheological instability criterion can be derived. When $\xi(\dot{\varepsilon}) < 0$, the material has rheological instability:

$$\xi(\dot{\varepsilon}) = \frac{\partial \ln[m/(m+1)]}{\partial \ln \dot{\varepsilon}} + m < 0. \tag{12}$$

Finally, in the coordinate system, temperature T is the abscissa and the logarithm of strain rate $\ln \dot{\varepsilon}$ is as the ordinate, contour curves of $\xi(\dot{\varepsilon})$ under different strain variables are drawn, and a rheological instability map can be obtained under different strains.

The power dissipation map and rheological instability map obtained by the above calculation are superimposed to obtain a processing map under different deformation conditions, as shown in Figure 13. As can be seen from the Figure, the stable thermal processing parameters of GH901 alloy were mainly focused on the deformation temperatures of 990–1070 °C, the strain rates of 0.001–0.17 s^{-1}, the deformation temperatures of 1070–1100 °C, and the strain rates of 0.001–0.6 s^{-1}. The deformation temperatures ranged from 1100 °C to 1140 °C and the strain rates ranged from 0.001–0.35 s^{-1}. According to the extreme value of power dissipation efficiency η, the optimal thermal processing parameters of GH901 alloy were as follows: deformation temperatures of 990–1030 °C, strain rates of 0.004–0.05 s^{-1}, and deformation temperatures of 1120–1140 °C, strain rates of 0.006–0.08 s^{-1}.

3.4. Numerical Simulation of Isothermal Forging

The structural size of GH901 superalloy plate forgings to be studied in this section is shown in Figure 14. The forging temperature of the alloy was 1090 °C. The billet measured Ø250 × 172 mm. The corresponding INCOLOY-901[1800–2050F (980–1120 °C)] was selected from the DEFORM material library for GH901 nickel-based superalloy. The constitutive equation of GH901 superalloy was introduced into the material model.

In the plastic forming process of alloys, there are commonly used classical models such as Coulomb friction model and shear friction model [24]. If the Coulomb friction model is used, the normal stress is generally greater than the yield stress of the material, and the friction stress obtained is often high, which results in the application of the model having great limitations. If the shear friction model is used, the friction stress only depends on the material's own characteristics, which is suitable for the plastic forming process under high stress state. In this study, the shear friction model was adopted, and the coefficient was set to 0.3 [25].

The workpiece was defined as a plastic body, and the upsetting and pressing of the upper and lower dies were defined as a rigid body. The number of grids, which were divided in the numerical simulation needed to be reasonable [26]; too much would increase the simulation time and reduce the work efficiency, and too little would lead to low accuracy and fail to meet the requirements. In this section, triangular meshes were used in the numerical simulation process, and 26,000 meshes were divided. Figure 15 is the 3D model diagram of the plate parts. Figure 16a,b are the results after the completion of numerical simulation of the two forming processes, respectively.
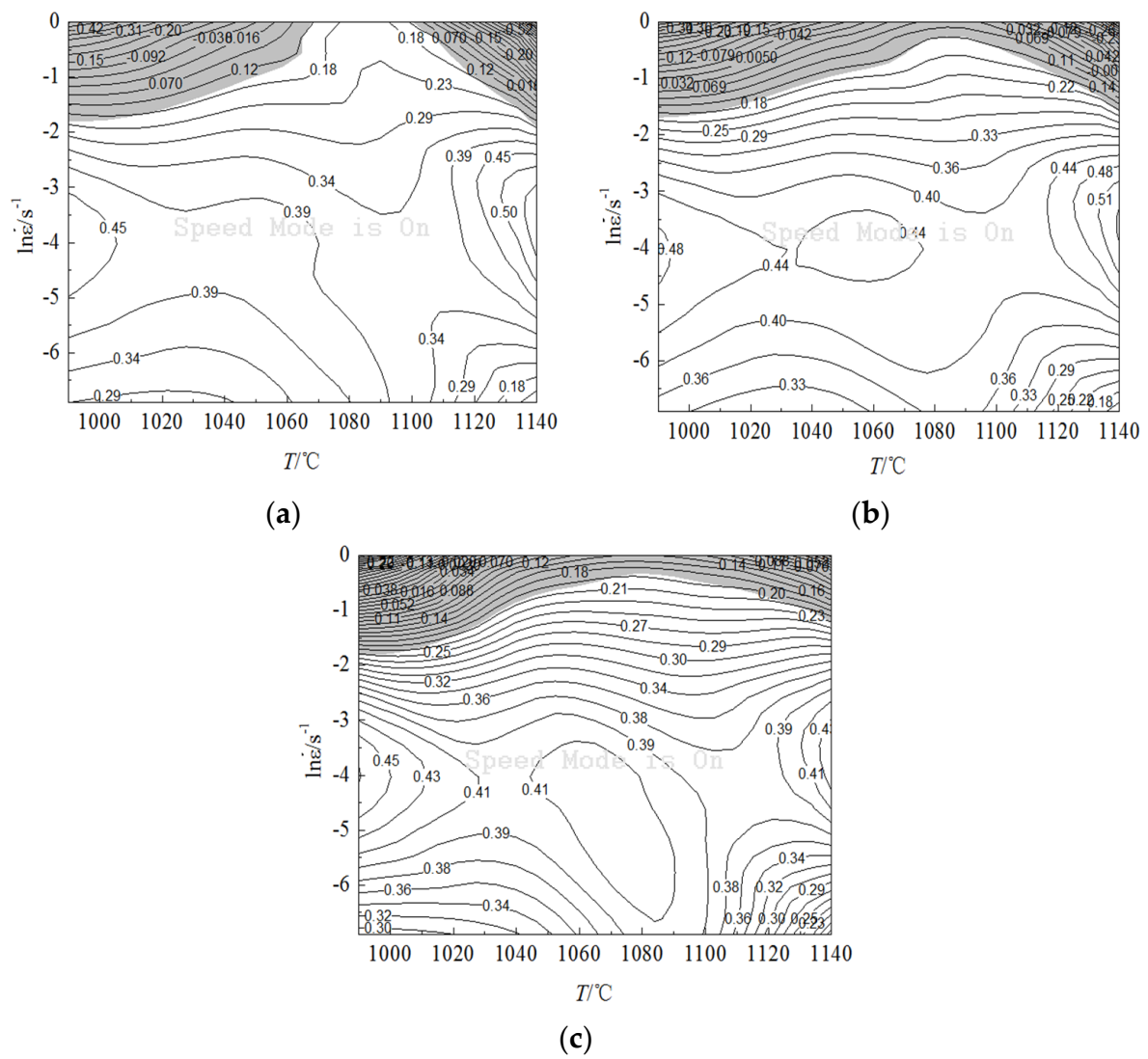
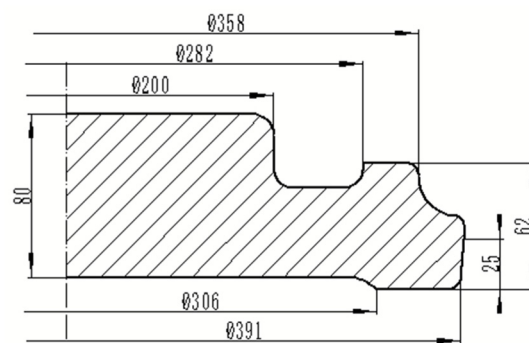**Figure 13.** Processing map of GH901 alloy under different strain variables. (**a**) $\varepsilon = 0.2$, (**b**) $\varepsilon = 0.4$, (**c**) $\varepsilon = 0.6$.

Figure 14. Plate forging.
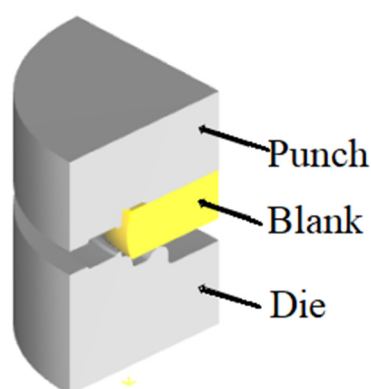
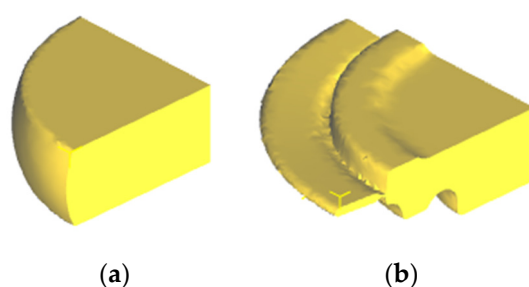**Figure 15.** 3D model of the disc.

(**a**)   (**b**)

Figure 16. Numerical simulation results. (**a**) Upsetting after billet, (**b**) disk forging.

Figure 17 showed the strain-rate nephogram of GH901 superalloy disk at a deformation temperature of 1090 °C. The blue figure in the upper right corner includes the shaft journal and wheel rim with a large bearing capacity. They were selected on the disk for stress analysis. Since the strain rate during the whole deformation process could not be guaranteed to be in the optimal processing range, the maximum bearing capacity was selected for testing. Figure 17 illustrates that the bearing capacity of the two reached the maximum value at 10.9 s. The average strain rates were 0.03 s^{-1} and 0.2 s^{-1}. They were in line with the reasonable thermal processing range determined by the processing map. The supporting evidence provided has proved that the optimum technological parameters obtained in this paper were reasonable. The forging produced by using this parameter is shown in Figure 18.
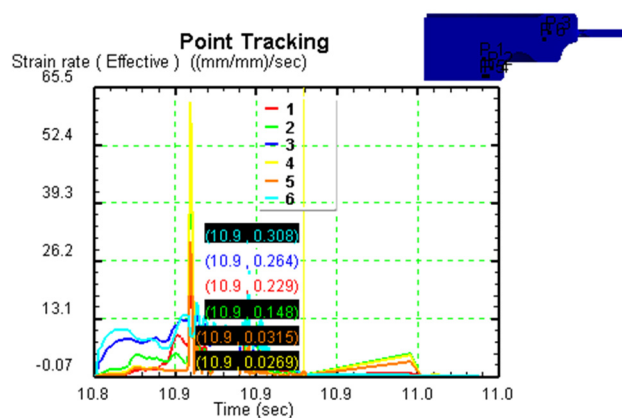

Figure 17. Strain-rate nephogram at the end of the molding process (deformation temperature is 1090 °C).

Figure 18. The final forgings produced.

4. Conclusions

Based on the thermal simulation experiments, the true stress–strain curves of GH901 superalloy under different deformation temperatures and strain rates were obtained. Processing maps of GH901 superalloy based on strain 0.3 and strain compensation were constructed. These showed that the hot deformation behavior of GH901 superalloy was related to the true strains, deformation temperatures and strain rates.

The stable thermal-processing parameters of GH901 superalloy mainly focused on the deformation temperatures of 990–1070 °C, the strain rates of 0.001–0.17 s^{-1}, the deformation temperatures of 1070–1100 °C, and the strain rates of 0.001–0.6 s^{-1}. The deformation temperatures ranged from 1100 °C to 1140 °C and the strain rates ranged from 0.001 to 0.35 s^{-1}. According to the extreme value of power dissipation efficiency η, the optimal thermal-processing parameters of GH901 superalloy were as follows: deformation temperatures of 990–1030 °C, strain rates of 0.004–0.05 s^{-1}, and deformation temperatures of 1120–1140 °C, and strain rates of 0.006–0.08 s^{-1}.

The results showed that the average strain rates of the journal and flange parts with a large bearing capacity were 0.03 s^{-1} and 0.2 s^{-1}, which were in accordance with the parameters selected by the processing map of the upper section. They were suitable for thermal processing of GH901 superalloy.

References

1. Zhang, C.; Shirzadi, A.A. Diffusion bonding of copper alloy to nickel-based superalloy: Effect of heat treatment on the microstructure and mechanical properties of the joints. *Sci. Technol. Weld. Join.* **2021**, *26*, 1–7. [CrossRef]
2. Wang, G.; Huang, L.; Zhao, P.; Zhan, X.; Qin, Z.; He, W.; Liu, F.; Nie, Y. Effect of Heat Treatment on Microstructure and Mechanical Properties of ODS Nickel-Based Superalloy via Strengthening Mechanism. *JOM* **2020**, *72*, 3279–3287. [CrossRef]
3. Eroglu, U. Perturbation approach to Eringen's local/non-local constitutive equation with applications to 1-D structures. *Meccanica* **2020**, *55*, 1119–1134. [CrossRef]
4. Zhu, L.W.; Xin, Y.P.; Wang, X.N.; Zhu, Z.S. Hot Compressive Behavior and Constitutive Equation of Ti-Al-Nb-Zr-Mo-Cr Alloy. *Mater. Sci. Forum* **2020**, *993*, 230–236. [CrossRef]
5. Ashtiani, H.; Shayanpoor, A.A. New constitutive equation utilizing grain size for modeling of hot deformation behavior of AA1070 aluminum. *Trans. Nonferrous Met. Soc. China* **2021**, *31*, 345–357. [CrossRef]
6. Yun, P.Z.; Pin, X.; Pei, P.J. Thermal deformation behavior and processing diagram of Mg-5Sn-2.5Pb magnesium alloy. *Trans. Mater. Heat Treat.* **2017**, *6*, 195–200.
7. Xu, D.Q.; Zhen, J.W.; Liang, T.; Chang, C.C.; Hong, P.S.; Yan, H. Study on hot deformation behavior and processing diagram of AZ91D magnesium alloy. *Spec. Cast. Nonferrous Alloy.* **2018**, *4*, 453–457.
8. Bo, L.; Wang, W.; Chen, C.; Hai, H.W.; Xi, C.Y.; Sun, Y. Hot compression deformation behavior of a new Ni-Cr-Co-Mo alloy. *Hot Work. Technol.* **2017**, *7*, 55–59.
9. Frost, H.J.; Ashby, F.M. Deformation-mechanism maps: The plasticity and creep of metals and ceramics. *Pergamon Press* **1982**, *9*, 265–276.
10. Raj, R. Development of a processing map for use in warm-forming and hot-forming processes. *Metall. Trans. A* **1981**, *12*, 1089–1097. [CrossRef]
11. Prasad, Y.V.R.K.; Gegel, H.L.; Doraivelu, S.M.; Malas, J.C.; Morgan, J.T.; Lark, K.A.; Barker, D.R. Modeling of dynamic material behavior in hot deformation: Forging of Ti-6242. *Metall. Trans. A* **1984**, *15*, 1883–1892. [CrossRef]
12. Prasad, Y.V. Author´s reply: Dynamic materials model: Basis and principles. *Metall. Mater. Trans. A* **1996**, *27*, 235–236. [CrossRef]
13. Prasad, Y.; Seshacharyulu, T. Modelling of hot deformation for microstructural control. *Int. Mater. Rev.* **1998**, *43*, 243–258. [CrossRef]
14. Gegel, H.L.; Malas, J.C.; Doraivelu, S.M.; Shende, V. Modeling techniques used in forging process design. *ASM Handb.* **1988**, *14*, 417–438.
15. Malas, J.C.; Seetharaman, V. Using material behavior models to develop process control strategies. *JOM* **1992**, *44*, 8–13. [CrossRef]
16. Alexander, J.; Lenard, J. *Modelling of Hot Deformation of Steels*; Springer: Berlin, Germany, 1989; pp. 105–115.
17. Bing, H.P. Effect of heat treatment on mechanical properties and grain size structure of GH901 alloy. *Spec. Steel Technol.* **2008**, *14*, 13–17.
18. Huan, Z.; Qing, L.; Guo, Z.; Jun, G.H.; Wen, Z.; Wen, J.L. Effect of heat treatment on microstructure and hardness of GH901 alloy. *Foundry Technol.* **2015**, *36*, 2643–2645.
19. Shao, L.D.; Jun, J.L. Effect of Forging Process on Wear Properties of GH901 Superalloy Turbine Shaft Forgings. *Hot Work. Technol.* **2017**, *21*, 109–112.
20. Yin, M.; Feng, D.; Han, G.W. Study on the Hot Working Process of Superalloy GH901. *Acta Metall. Sin.* **1999**, *35*, 24–27.
21. Shore, F.M.; Morakabati, M.; Abbasi, S.M.; Momeni, A. Hot Deformation Behavior of Incoloy 901 through Hot Tensile Testing. *J. Mater. Eng. Perform.* **2014**, *23*, 1424–1433. [CrossRef]
22. Shore, F.M.; Morakabati, M.; Abbasi, S.M.; Momeni, A.; Mahdavi, R. Hot Ductility of Incoloy 901 Produced by Vacuum Arc Remelting. *ISIJ Int.* **2014**, *54*, 1353–1360. [CrossRef]
23. Li, X.; Li, X.; Zhou, H.; Zhou, X.; Li, F.; Liu, Q. Simulation of dynamic recrystallization in AZ80 magnesium alloy using cellular automaton. *Comput. Mater. Sci.* **2017**, *140*, 95–104. [CrossRef]
24. Long, W.G. Research on New Forming Technology of High Pressure Elbow with Straight Section. *Qinhuangdao Acad. Pap. Yanshan Univ.* **2017**, *4*, 15–20.
25. Li, F.M.; Cheng, L.H.; Zhen, Z. Research progress of friction model in metal plastic forming. *Die Mould. Ind.* **2014**, *4*, 1–7.
26. Dong, S. Research on Finite Element Meshing Applied to 3D-IC. *Diss. Dalian Univ. Technol.* **2009**, *7*, 33–36.